5.8 X-ray Calorimeters

F. Scott Porter

NASA Goddard Space Flight Center

Abstract

X-ray calorimeter instruments for astrophysics have seen rapid development since they were invented in 1984. The prime instrument on all currently planned X-ray spectroscopic observatories is based on calorimeter technology. This relatively simple detection concept that senses the energy of an incident photon by measuring the temperature rise of an absorber material at very low temperatures, can form the basis of a very high performance, non-dispersive spectrometer. State-of-the-art calorimeter instruments have resolving powers of over 3000, large simultaneous band-passes, and near unit efficiency. This coupled with the intrinsic imaging capability of a pixilated x-ray calorimeter array, allows true spectral-spatial instruments to be constructed. In this chapter I briefly review the detection scheme, the state-of-the-art in X-ray calorimeter instruments and the future outlook for this technology.

Introduction

An X-ray calorimeter is a conceptually simple device that provides simultaneous spatial and spectral observations for X-ray astrophysics. Current X-ray observatories use charge coupled devices CCDs and precision focusing optics to achieve high spatial resolution but with limited inherent spectral resolution. High-resolution spectroscopy is achieved with dispersive optics and position sensitive detectors. Dispersive optics are additionally constrained by relatively low efficiency and a limited bandpass. Moreover, the performance degrades for objects larger than the point-spread function of the optics. In contrast, an X-ray calorimeter provides a broad-band, high resolution spectrometer with inherent imaging capability where every pixel in a pixilated focal plane is a high resolution spectrometer. In addition, the performance of a calorimeter is not affected by the spatial extent of the source and is insensitive to polarization.

As in all branches of astrophysics, spectroscopy is the key to isolating the physical interactions occurring in a celestial source. X-ray spectroscopy, in particular, yields information on the composition, temperature, ionization equilibrium, density, and bulk and turbulent motion, of the X-ray emitting plasmas that make up the bulk of the observable matter in the Universe. Specifically, X-ray spectroscopy probes, for example, accretion around black holes and active galactic nuclei, shock heated plasmas in stellar winds and supernova remnants, mergers of clusters of galaxies, and the decay processes in γ-ray burst. In addition, X-ray back-lighting and photo-ionization provide key diagnostics of the intervening material between the observer and cosmic X-ray sources. With current X-ray observatories, high-resolution spectroscopy is limited to a handful of the brightest sources and only over a limited spectral range concentrated below 2 keV. All major X-ray observatories planned for the next decade including *Spectrum-Röntgen-Gamma (SRG)*, *Astro-H*, and the *International X-ray Observatory (IXO)*, include a calorimeter system as one of the primary focal-plane instruments. In this chapter, we briefly review the operating concepts behind a calorimeter instrument, the current state of the art in detector systems, current and future spaceflight instruments, and prospects for future large scale imaging spectrometers. A complete development of calorimeter theory is given in Mather (1982), Moseley et al (1984), and McCammon (2005).

The basic concept of a calorimeter is shown in Figure 1, consisting of an X-ray absorber, a sensitive thermometer, and a heat sink held at low temperature, typically below 0.1 K. Figure 2 shows a spaceflight detector with its components labeled. Incident X-rays are photo-absorbed in the X-ray absorber at temperature T, releasing a primary photo-electron and one or more Auger electrons. The liberated electrons then thermalize into the available energy reservoirs in the solid-state system at a higher temperature T'. Phonon-states in an insulator, phonon and electronic states in a metal, and phonon and quasi-particle states in a superconductor dominate the thermalization channels, although more exotic reservoirs can also contribute. The change in temperature as a function of energy is then simply governed by the heat capacity of the system as

$$\Delta T = T' - T \approx \frac{E}{C(\bar{T})} \qquad (1)$$

where E is the energy of the incident photon and C is the heat capacity of all contributing states in the absorber. A thermometer placed in good thermal contact with the absorber then senses the change in temperature and thus the energy of the incident photon through the simple relationship (1). Finally, a weak thermal link to the heat sink returns the detector to its base temperature for the next photon interaction. An example of the thermal response for a detector from a 6 keV X-ray is shown in Figure 3. An arbitrarily sensitive thermometer with infinite dynamic range coupled to an arbitrarily small heat capacity, has no upper limit to the spectral resolving power. As we shall see, practical considerations and specific instrument requirements generally limit the performance of the detector system.

Calorimeters are intrinsically imaging in a pixilated detector. For example, Figure 4 shows a calorimeter array built for the X-ray Quantum Calorimeter (XQC) sounding rocket with 36 detector elements. Coupled with focusing X-ray optics, the detector channels are completely independent, both spatially and spectrally, yielding an X-ray image where each imaging element is an independent high-resolution spectrometer. Larger imaging arrays, including the 4096 element *IXO* detector, are currently in development, and even larger megapixel arrays are planned for the future. As a spatial-spectral instrument, the calorimeter detector is similar and complementary to an X-ray CCD. The spectral resolution of an X-ray CCD is fundamentally limited by the counting statistics of charges formed in the cascade from an X-ray liberated photoelectron to carriers at the band-gap of the material. This gives them moderate spectroscopic resolving power of about 50 at 6 keV. On the other hand, CCDs scale to very large imaging arrays because one can easily transfer the X-ray initiated charge cloud from the interaction site to collection nodes on the exterior of the array. For calorimeters the situation is inverted. The spectral resolving power has no fundamental limit, and practical detectors have achieved resolving powers of 3000 at 6 keV, but the array size is limited by our ability to fabricate detector arrays with individually wired single or small groups of pixels. No analog to the charge transfer mechanism in CCDs has been invented for a thermal detector.

An example of the relative performance of a calorimeter array is shown in Figure 5 for a simulated observation of M82 along with a simulated CCD observation of the same object. A real-world example is shown in Figure 6 where a plasma of He-like and H-like iron was observed using the EBIT calorimeter

spectrometer (ECS) calorimeter instrument at the Lawrence Livermore National Laboratory (Porter et al 2008a).

In practical detectors, the performance of a calorimeter is limited by both extrinsic noise such as amplifier and photon shot noise, and intrinsic noise such as Johnson noise and thermodynamic noise. Thermodynamic noise, which is the thermal noise associated with energy exchange across the weak thermal link shown in Figure 1, fundamentally limits the resolving power of the detector. For an optimized detector this is given for $\alpha >> 1$ as:

$$\Delta E \propto \sqrt{\frac{k_B T_0^2 C_0}{\alpha}} \qquad (2)$$

where T_0 is the temperature of the heat sink, C_0 is the heat capacity at that temperature, k_B is Boltzmann's constant, and α is a measure of the thermistor responsivity (Moseley et al 1984, McCammon 2005). High spectroscopic resolution is generally achieved by running at very low bath temperatures, usually < 100 mK, with small, low heat capacity systems, and high responsivity thermometers. In designing a practical detector, other noise sources in the system are minimized with respect to the thermodynamic noise to achieve the highest possible spectral resolving power.

Calorimeter detectors

Over the last two decades, the field has seen rapid development in the United States, Europe, and Japan. Current calorimeter research concentrates on three main components of the technology, the thermistor design, the absorber design, and the readout system.

X-ray calorimeter detectors can encompass a huge performance phase space that includes spectral resolving power, counting rates, detector size, and dynamic range (bandpass). Optimizing for a specific set of instrument requirements is a highly coupled problem, and most of the optimization phase space is unexplored. Two examples of very different optimizations illustrate this point. Figure 4 shows the detector array for the X-ray Quantum Calorimeter (XQC) sounding rocket experiment. It is a 36-pixel device with very large (2 mm x 2 mm) pixels and an energy resolution of 7 eV at 1.5 keV. The detector is optimized for low energies up to about 1 keV. However, the large size of the absorber limits the thickness and thus the bandpass over which it has high

quantum efficiency. In contrast, high-energy detectors with thicker, more opaque absorbers, have been optimized for energies up to 100 keV with energy resolutions of around 25 eV at 60 keV (Doriese et al 2007; Porter et al 2008b). The high-energy detector is optimized for dynamic range at the expense of both energy resolution and speed. The low energy detector was optimized differently, emphasizing detector area and energy resolution over dynamic range. Many other optimizations are possible including optical detectors with a dynamic range of a few electron volts (see for example, Romani et al 2001), alpha particle detectors with a dynamic range of several million electron volts (Horansky et al 2008), and high cadence solar X-ray detectors with small but very fast pixels. Detector optimization, however, is highly dependent on the underlying calorimeter technology where some component choices lend themselves more easily to certain applications.

Calorimeters are usually classified by the choice of thermistor technology, which generally drives the design of the rest of the detector array and the instrument as a whole. Table 1, gives an overview of the major thermistor technologies and how they cascade into a few of the other system parameters. Detectors based on semiconductor thermistors (McCammon 2005b) are the most mature and have been optimized for a wide variety of applications. Semiconductor thermistors have relatively low responsivity, usually specified as:

$$\alpha \equiv \frac{d\log(R/\Omega)}{d\log(T/K)} \qquad (3)$$

where R is the resistance, T is the temperature, and alpha is generally less than 10 for a semiconductor thermistor. However, with a careful choice of absorber material, extremely high performance detectors can be constructed. Figure 7 shows a spectrum of a ^{55}Fe radioactive source using a 400 μm x 400 μm detector with 95 % quantum efficiency at 6 keV giving a spectral resolving power of almost 2000. A spectrum using a device optimized for high energies is also shown in Figure 7 giving a resolving power of over 2000 at 60 keV in an array of 500 μm x 500 μm pixels with 32 % quantum efficiency at 60 keV. Semiconductor thermistors are generally read out by cooled junction field effect transistors (JFETs) (Porter et al 1999) and are operated at high impedance to minimize the contributions of amplifier noise. The high impedance of the detectors and the use of JFET amplifiers severely limits the size of the focal plane arrays. Most

semiconductor detector arrays are less than 100 pixels, although the HAWC infrared bolometer array for the Sofia airborne observatory has 384 cryogenic JFET readout channels (Harper 2004), and a 256-pixel X-ray detector is being developed at GSFC.

Newer thermistor technologies allow for easier access to other regions of the detector optimization space and expand the range of accessible absorber materials. Specifically, transition-edge sensor (TES) calorimeters are the leading candidate for the *IXO* observatory that is expected to launch around 2018-2020. Transition-edge thermistors use a superconductor that is biased in the middle of a very narrow normal-superconducting transition. A TES thermistor has a very high responsivity with an α between 100 and 1000, but over a fairly narrow temperature range, generally less than 1 mK for temperatures near 100 mK. From equation 2, one can see that a high α can lead to increased energy resolution. However, a high α also leads to a much greater range of allowable heat capacities, and thus, in principle, a greater range of acceptable absorber materials. TES thermistors are voltage biased, where the Joule power dissipated in the thermistor heats the device into its transition. This is a stable bias point for a thermal detector since the absorption of energy increases the resistance of the device, thus decreasing the Joule power dissipation and keeping the TES near its bias point. In operation, the device is biased to a temperature well above the bath temperature, generally ≈100 mK for a 50 mK bath temperature. The large temperature gradient, and the decrease in bias power during an X-ray event, vastly improves the detector recovery time. This has been termed "extreme electro-thermal feedback". A similar, though smaller, effect occurs with semiconductor thermistors. TES detector systems have achieved excellent energy resolution across a wide range of optimizations. An example is shown in Figure 8 for a 250 μm x 250 μm pixel that gives a resolving power of almost 3000 at 6 keV (Iyomoto et al 2007).

Semiconductor and TES calorimeters have received the most development funding for the longest period of time and are thus the most technologically evolved thermistor technologies. Newer systems using magnetic susceptibility thermistors (Fleischmann et al 2005) and kinetic inductance thermistors (Mazin et al 2008) are again broadening the phase space for detector optimization. Both of these technologies may lend themselves to very large detector arrays, approaching 10^6 pixels.

The thermistor chosen for the detector system drives the readout technology that ultimately drives the complexity and scalability of the instrument. Semiconductors are well matched to JFET front-end amplifiers that must be placed in close proximity to the detector array to prevent microphonic pickup noise in the wiring to the high impedance detectors. A typical semiconductor readout circuit, with its complex thermal staging, is shown in Figure 9. TES detectors, in contrast, are low impedance devices that are well matched to a current sensing superconducting quantum interference device (SQUID) amplifier. SQUIDs are high sensitivity, low power, amplifiers that operate at cryogenic temperatures and are well suited to calorimeter instruments.

An important advantage of SQUID readout systems is that several high-density (Kiviranta et al 2002; Reintsema et al 2003; Irwin et al 2006) readout systems have been developed. These readout systems combine multiple pixels onto a single readout node, significantly reducing the wiring complexity of a detector array. For example, Figure 10 shows a schematic for a SQUID based time division multiplexer (TDM) developed at the National Institute of Standards and Technology that implements row-column readout. In the TDM system, front-end SQUIDs on the focal plane sample a column of detector channels using a single output amplifier. This is akin to a typical commercial laboratory digitizer where a number of inputs are multiplexed to a single amplifier and analog-to-digital converter. The result is a major improvement in the wiring complexity of an N x N array, where the wiring scale goes from O(N^2) to O(N) vastly simplifying the instrument design. A 4 column by 32 row NIST TDM multiplexer system with a NASA/GSFC 8x8 TES detector array is shown in Figure 11.

Spaceflight Calorimeter Instruments

X-ray calorimeters have a relatively short spaceflight history but the number of planned near-term instruments is quite large. These are summarized in Table 2. Here we briefly describe the *XQC* and *Suzaku/XRS* instruments as examples of adapting a complex calorimeter detector systems to a space environment. In the next section, we discuss future missions including *Astro-H* and *IXO* where mission requirements define the majority of current calorimeter research.

The *XQC* instrument was the first calorimeter instrument in space and has flown four times on a suborbital sounding rocket since 1995. The instrument is designed without focusing optics to measure the detailed spectral structure of the soft X-ray background. The results have shown that the ubiquitous soft X-ray emission that dominates the X-ray sky is largely composed of individual emission lines that are almost certainly due to a superposition of geospheric and heliospheric charge exchange emission and line emission from the local interstellar medium (McCammon et al 2002). The *XQC* instrument is a good model of a spaceborne calorimeter since it encompasses all aspects of an orbital instrument except a long duration cryogenics system, but with the added complexity of very high vibration loads, and the requirement to achieve operational equilibrium within 60 s of launch (Porter et al 2000).

The *XQC* uses an implanted silicon semiconductor detector array that operates at 50 mK with an individual JFET amplifier per channel operated at 130 K. The cryostat uses 4 L of liquid helium pumped to 1.6 K to precool an adiabatic demagnetization refrigerator (ADR) that uses a 50 g ferric ammonium alum (FAA) salt pill in a 4 T superconducting magnet to reach 50 mK. The most recent flight (April, 2008) used the new 36 pixel detector array shown in Figure 4 (McCammon et al 2008). The *XQC* detector array is monolithically fabricated using micromachined silicon with the semiconductor thermistors formed in-situ using ion-implantation. The absorbers are 0.8 μm of HgTe epitaxially grown on a silicon backing layer that are then epoxied to spacer posts on the pixel. The new *XQC* array uses very large 2 mm x 2 mm pixels to give a total collecting area of 1.44 cm^2 and has a resolution of 7 eV FWHM at 1.5 keV during ground testing.

The XRS2 instrument on the *Suzaku* observatory uses technology very similar to the *XQC* but was developed for long-term operation in space (Kelley et al 2007). The original XRS instrument was launched on the *Astro-E* observatory in 1999 but did not reach orbit due to a failure of the first stage booster. The XRS instrument on *Suzaku* was launched in 2005 and worked flawlessly until the cryogens were prematurely exhausted due to an instrument accommodation error on the spacecraft five weeks after launch. So far, the XRS2 is our only experience with an orbital calorimeter instrument, successfully demonstrating many of the supporting technologies that will be used on future calorimeter instruments.

The XRS2 used a 6x6 calorimeter array fabricated using the same process as the array in the XQC instrument but with a different optimization (Stahle et al 2004). The pixel size of the XRS is smaller at 0.625 mm x 0.625 mm but the HgTe absorber material is ten times thicker. This extends the bandpass of the instrument to above 10 keV with high quantum efficiency and yields an energy resolution, on orbit, of 7 eV FWHM at 6 keV (Kelley et al 2007). The XRS used a four stage cooler to reach its 60 mK operating temperature consisting of a 100 K mechanical cryocooler, 120 L of solid Neon at 17 K, 32 L of space-pumped superfliud helium at 1.3 K, and an ADR at 60 mK. The ADR is relatively large with 920 g of FAA in a 2 T superconducting magnet, but it contains no moving parts and had a hold time, on orbit, of ~36 h with a 1 h recharge. An important legacy of the XRS2 instrument is the onboard data processing system that analyzed each X-ray event using an "optimal" digital filter to estimate the X-ray energy (Boyce et al 1999). Only the processed event list was telemetered to the ground. This is necessary to reduce the very large intrinsic data rate of the instrument (6.3 Mbit/s for XRS, ≈ 6.4 Gbit/s for *IXO*) to the < 100 kbit/s average data rate typically available on orbit. Future calorimeter missions will likely use a variant of this system.

The XRS detector system continues to be an important technology for X-ray astrophysics. A ground-based version of the instrument has been operating almost continuously at the Electron Beam Ion Trap (EBIT) at Lawrence Livermore National Laboratory since 2000 making fundamental measurements of astrophysical plasmas in the laboratory (Porter et al 2000, 2008b). In addition, the flight spare XRS detector system is being considered for flight on the *Spectrum-Röntgen-Gamma (SRG)* observatory to be launched in 2011, and a similar detector system, with improved performance, will be flown on the *Astro-H* observatory in 2013.

Future Spaceflight Instruments

Beyond the near term *SRG* and *Astro-H* observatories mentioned in the previous section, most calorimeter development is targeted for the *IXO* mission. This large orbiting observatory has a long (>20m) focal length with precision X-ray optics that place severe constraints on the focal plane instruments. For example, oversampling the 5" point-spread-function of the *IXO* telescope requires

5" pixels that are less than 416 μm x 416 μm in size. To cover the required 5' field-of-view (FOV) then requires a 4096-element imaging array. The instrument's FOV is extremely important, providing crucial spatial information for diffuse objects, and critical background information for point sources. For example, the FOVs for *Suzaku*/XRS and *IXO*/XMS (X-ray Microcalorimter Spectrometer) are shown in Figure 12 in comparison to a large, diffuse galaxy cluster. To achieve these large array sizes, calorimeter development has centered on monolithically fabricated TES arrays with multiplexed readouts.

Semiconductor calorimeters are well developed, space-flight qualified, and are likely to achieve the spectral resolution requirements for the *IXO* mission. However, the arraying and readout technologies do not scale well beyond a few hundred channels. TES detectors are now being fabricated in fairly large arrays, currently 8 x 8 (Iyomoto et al 2008) and will scale to 32 x 32 in the next year. These arrays are being instrumented successfully with multiplexed readouts, with one such example shown in Figure 11. Importantly, small scale science instruments using this technology are already being constructed. These include the EURECA TES synchrotron experiment, shown in Figure 13, that will be a test-bed for candidate *IXO* detectors and frequency domain multiplexing (de Korte et al 2008), the Transition-Edge Microcalorimeter Spectrometer (TEMS) that will be deployed at EBIT (Porter et al 2008a), and the *Micro-X* sounding rocket experiment which will observe the Puppis A supernova remnant with a 11x11 multiplexed TES array in 2011 (Figueroa-Feliciano et al 2008).

Outlook

X-ray calorimeter technology has progressed substantially since its inception in 1984 with ground and first generation spaceflight instruments already in operation. Near term missions such as *SRG* and *Astro-H* will use improved versions of these instruments and the technology is well advanced for the next-generation instrument that will be deployed on the *IXO* Observatory. These missions will provide exceptional spectrometers with very high sensitivity, enabling routine, high-resolution spectroscopic observations of nearly every class of X-ray emitting object.

Future missions such as the *Generation-X* (Windhorst et al 2006) and *MAXIM* (Gendreau et al 2004) mission concepts will require much larger detector

arrays to match their precision (< 0.1") optics with a reasonable field of view. Scaling the current arraying and readout technologies to this level will be challenging at best. The most likely scenario for achieving megapixel calorimeter arrays is to adopt detector elements that are spatially sensitive and also to adopt a readout technology that can pack a very high density of detector channels per readout node. Position sensitive TES detectors have been under development for several years (Figueroa-Feliciano et al 2006; Smith et al 2006), and have shown that for a modest degradation in detector performance, sub-pixel position information can be encoded in the detector response. In addition, microwave SQUID circuits are being developed to pack large numbers of TES detectors on to a single high-bandwidth readout node (Irwin et al 2006).

Newer calorimeter technologies may also play a large role in achieving megapixel scale arrays. Magnetic calorimeters are dissipation-less systems that substantially improve the very serious problem of thermal management on a large detector array. Kinetic Inductor detectors have both sub-pixel position resolution and are readout in a high-Q microwave resonance circuit that can pack several thousand channels onto a single readout node.

The future of X-ray calorimeter spectrometers is exciting with a number of near-term missions ready to move from development into implementation. The long-term future of X-ray astrophysics, however, will require precision X-ray optics and matching imaging spectrometers with large fields of view and very high spectral resolution. The challenge will be to find clever new ways to package and instrument calorimeter arrays on this much larger scale.

Acknowledgements: The author wishes to thank the X-ray detector development groups at the Goddard Space Flight Center, the National Institute of Standards and Technology, and the Netherlands Institute for Space Research for providing material, and the National Aeronautics and Space Administration for financial support for this work.

References:

Mather, J.C.: (1982) Bolometer noise: nonequilibrium theory. Appl. Opt. **21** ,1125-1129 (1982)

Moseley, S.H, Mather, J.C., McCammon, D.: Thermal detectors as x-ray spectrometers. J. Appl. Phys. **56**, 1257-1262 (1984).

McCammon, D.: Thermal Equilibrium Calorimeters – An Introduction. In: Enss, C. (ed) Cryogenic Particle Detection, pp 1-34. Springer, Berlin Heidelberg New York (2005a)

McCammon, D.: Semiconductor Thermistors. In: Enss, C. (ed) Cryogenic Particle Detection, pp 35-61. Springer, Berlin Heidelberg New York (2005b)

Porter, F.S., Beiersdorfer, P., Brown, G.V., et al.: The EBIT Calorimeter Spectrometer: A New, Permanent User Facility at the LLNL EBIT. J. Low Temp. Phys. **151**, 1061-1066 (2008a)

Porter F.S., Beck, B.R., Beiersdorfer, P., et al.: The XRS microcalorimeter spectrometer at the Livermore electron beam ion trap. Can .J. Phys. **86**, 231-240 (2008b)

Doriese, W.B., Ullom, J.N., Beall, J.A., et al.: 14-pixel, multiplexed array of gamma-ray microcalorimeters with 47 eV energy resolution at 103 keV. Appl. Phys. Lett. **90**, 193508 (2007)

Romani, R.W., Miller, A.J., Cabrera, B., et al.: Phase-resolved Crab Studies with a Cryogenic Transition-Edge Sensor Spectrophotometer. ApJ **563**, 221-228 (2001)

Horansky, R.D., Ullom, J.N., Beall, J.A., et al.: Analysis of Nuclear Material by Alpha Spectroscopy with a Transition-Edge Microcalorimeter. J. Low Temp. Phys. **151**, 1067-1073 (2008)

Porter, F.S., Audley, M.D., Brokosky, R., et al.: The Detector Assembly and the Ultra Low Temperature Refrigerator for XRS. Proc. SPIE **3765**, 729-740 (1999)

Harper, D.A. Bartels, A.E., Casey, S.C., et al.: Development of the HAWC far-infrared camera for SOFIA. Proc. SPIE **5492,** 1064-1073 (2004)

Iyomoto, N., Bandler, S.R., Brekosky, R.P., et al.: Close-packed arrays of transition-edge x-ray microcalorimeters with high spectral resolution at 5.9 keV. Appl. Phys. Lett. **92,** 013508 (2008)

Mazin B.A., Eckart, M.E., Bumble, B., et al.: Optical/UV and X-Ray Microwave Kinetic Inductance Strip Detectors. J. Low Temp. Phys. **151**, 537-543 (2008)

Kiviranta, M., Seppa, H., van der Kuur, J. et al.: SQUID-based readout schemes for microcalorimeter arrays. AIP Conf. Proc. **605**, 295-300 (2002)

Reintsema, C.D., Beyer, Jörn; Nam, Sae Woo, et al.: Prototype system for superconducting quantum interference device multiplexing of large-format transition-edge sensor arrays. Rev. Sci. Inst. **74**, 4500-4508 (2003)

Irwin, K.D., Beall, J.A., Doriese, W.B., et al.: Microwave SQUID multiplexers for low-temperature detectors. NIMPA **559**, 802-804 (2006)

McCammon, D., Almy, R., Apodaca, E., et al.: A High Spectral Resolution Observation of the Soft X-Ray Diffuse Background with Thermal Detectors. ApJ **576**, 188-203 (2002)

Porter, F.S., Almy, R., Apodaca, E., et al.: The XQC microcalorimeter sounding rocket: A stable LTD platform 30 seconds after rocket motor burnout. NIMPA 444:220-223 (2000)

McCammon, D., Barger, K., Brandl, D.E., et al.: The X-ray Quantum Calorimeter Sounding Rocket Experiment: Improvements for the Next Flight. J. Low Temp. Phys. **151**, 715-720 (2008)

Kelley, R.L., Mitsuda, K., Allen, C.A., et al.: The Suzaku High Resolution X-Ray Spectrometer. PASJ **59**, 77-112 (2007)

Stahle, C.K., Allen, C.A., Boyce, K.R., et al.,: The next-generation microcalorimeter array of XRS on Astro-E2. NIMPA **520**, 466-468 (2004)

Boyce, K.R., Audley, M.D., Baker, R.G., et al.: Design and performance of the ASTRO-E/XRS signal processing system. Proc. SPIE **3765**, 741-750 (1999)

Porter, F.S., Audley, M.D., Beiersdorfer, P., et al.: Laboratory Astrophysics using a Spare XRS Microcalorimeter. Proc. SPIE **4140**, 407-418 (2000)

de Korte, P., Anquita, J., Bakker, F., et al.: EURECA – European-Japanese microcalorimeter array. J. Low Temp. Phys. **151**, 733-739 (2008)

Figueroa-Feliciano, E., Bandler, S.R., Bautz, M., et al.: Micro-X: Mission Overview and Science Goals. J. Low Temp. Phys. **151**, 740-745 (2008)

Windhorst, R.A., Cameron, R.A., Brissenden, R.J., et al.: Generation-X: An X-ray observatory designed to observe first light objects. New Astron. Rev. **50**, 121-126 (2006)

Gendreau, K.C., Cash, W.C., Gorenstein, P., et al.: MAXIM: the black hole imager. Proc. SPIE **5488**, 394-402 (2004)

Figueroa-Feliciano, E., Bandler, S.R., Boyce, K., et al.: Expanding the Constellation-X field of view with position-sensitive x-ray microcalorimeters. Proc. SPIE **6276**, 627615 (2006).

Smith, S.J., Whitford, C.H., Fraser, G.W.: Signal processing for distributed readout using TESs. NIMPA **559**, 814-816 (2006)

Porter, F.S., Kelley, R.L., Kilbourne, C.A.: High resolution X-ray microcalorimeters. NIMPA **559**, 436-438 (2006)

Table 1. Classes of X-ray calorimeters by thermistor technology for Semiconductor, Transition Edge Sensor (TES), Metallic Magnetic Calorimeter (MMC), and Microwave Kinetic Inductance Detector (MKID) detector schemes. MKIDs, while not strictly equilibrium thermal detectors, show huge promise for future megapixel detector arrays.

	Semiconductor	TES	MMC	MKID
Physical effect	Mott Hopping	Normal-superconducting transition	Magnetic susceptibility	Quasi-particle modulated impedance
Readout	JFET	SQUID	SQUID	Microwave resonator
Temperature	50 to 100 mK	50 to 100 mK	50 to 100 mK	50 to 100 mK
Pixel size	0.5 to 2.0 mm	0.05 to 1.0 mm	0.05 to 0.5 mm	0.2 mm strip
Multiplexable	Not yet	Yes	Yes	Yes
Best ΔE at 6 keV	3.2 eV	2.1 eV	2.7 eV	62 eV
Demonstrated bandpass	0.02 to 100 keV	1 eV to 5 MeV	100 eV to 5 MeV	0.03 to 6 keV

Table 2. Current and planned space-borne calorimeter instruments. Launch dates and performance of future missions are best estimates from publicly accessible data.

Mission	launch	Technology	Array size (pixels)	Pixel size (mm)	Bandpass (keV)	Resolution (eV FWHM)
XQC1	1995-1999	Semi.	2x18	0.5x2.0	0.05 to 3	8 @ 1 keV
XQC2	2008 -	Semi.	6x6	2.0x2.0	0.05 to 3	7 @ 1.5 keV
Astro-E	1999	Semi.	2x18	0.25x1.0	0.3 to 10	11 @ 6 keV
Suzaku	2005	Semi.	6x6	0.63x0.63	0.3 to 10	7 @ 6 keV*
SRG	2011	Semi.	6x6	0.82x0.82	0.3 to 10	4 @ 6 keV
Astro-H	2013	Semi.	8x8	0.82x0.82	0.3 to 10	4 @ 6 keV
Micro-X	2011	TES	11x11	0.5x0.5	0.1 to 3	2 @ 2 keV
IXO‡	2020	TES	64x64	0.25x0.25	0.3 to 12	2 @ 6 keV

* On orbit performance.

‡ *IXO* is the merger of the U.S. Constellation-X and the European XEUS missions.

Figure Legends:

Figure 1. A Schematic view of a calorimeter detector. An incoming X-ray is photo-absorbed in the absorber and the resultant equilibrium thermal signal is registered with a sensitive thermometer. The detector is thermally reset to the heat sink temperature through a weak thermal link.

Figure 2. An XRS spaceflight calorimeter detector without the absorber (left) and after the 8 μm thick HgTe absorber is attached (right) (Stahle et al 2004). The absorbers are 624 μm x 624 μm.

Figure 3. The thermal signature of an individual X-ray as measured by the semiconductor calorimeter shown in Figure 2. The incident 6 keV X-ray produces a 5 mK temperature rise in the detector before it relaxes to its equilibrium state through the weak thermal link to the heat sink.

Figure 4. The 36 pixel calorimeter array for the X-ray Quantum Calorimeter (XQC) sounding rocket instrument. Each X-ray absorber is 2 mm x 2 mm x 0.8 μm (McCammon et al 2008).

Figure 5. A simulated spectrum of the starburst galaxy M82 (inset, Credit: NASA/CXC/SAO/PSU/CMU) using the proposed NeXT calorimeter array. A simulated lower resolution spectrum for an X-ray CCD instrument is also shown (R. Smith, personal communication, 2008).

Figure 6. A measurement of highly charged H-like and He-like iron measured with the EBIT Calorimeter Spectrometer (ECS) at the Electron Beam Ion Trap (EBIT) facility at the Lawrence Livermore National Laboratory. The ECS is a production spectrometer based on the *Suzaku*/XRS calorimeter instrument (Porter et al 2008a).

Figure 7. (left) A Mn K_α spectrum measured with a semiconductor calorimeter array giving 3.2 eV FWHM spectral resolution at 5.9 keV. The X-ray absorbers were 400 μm x 400 μm x 8 μm of HgTe with 95 % quantum efficiency at 6 keV (Porter et al 2006). (right) A spectrum of the 60 keV emission line from ^{241}Am measured with a high energy semiconductor calorimeter array giving 22 eV FWHM spectral resolution at 60 keV. The X-ray absorbers were 500 μm x 500 μm x 100 μm of HgTe with 32 % quantum efficiency at 60 keV (Porter et al 2008b).

Figure 8. A Mn K_α spectrum measured with a Transition-Edge (TES) calorimeter array giving 2.4 eV FWHM spectral resolution at 5.9 keV. The X-ray absorbers were 250 μm x 250 μm x 5.3 μm of Au with 99 % quantum efficiency at 6 keV (Iyomoto et al 2008).

Figure 9. A standard readout circuit for a semiconductor calorimeter detector. The detector is current biased through a large load resistor and read-out with a cryogenic JFET source follower that is placed in close proximity to the detector. This specific circuit is from the *Suzaku*/XRS instrument (Kelly et al 2007).

Figure 10. A time division multiplexer (TDM) readout circuit for a TES calorimeter instrument (Doriese et al 2007). The TDM is a row-column system where front-end SQUIDS are commonly addressed for each row with the outputs for all the SQUIDS in a column combined on to a single output amplifier. This decreases the wiring complexity from O(N^2) to O(N) for an N x N detector array. A 1024 pixel array could be readout with a 32 column x 32 row multiplexer.

Figure 11. A test fixture for a TDM multiplexer and TES calorimeter array. The TDM is a NIST 4 column by 32 row multiplexer (Doriese et al 2007) with a NASA/GSFC 8x8 TES calorimeter array in the center (Iyomoto et al 2008). The array pixels are 250 μm x 250 μm each.

Figure 12. An X-ray image of the Fornax galaxy cluster observed with *ROSAT*. The fields-of-view (FOV) for the *Suzaku*/XRS and *IXO*/XMS are overlaid on the image. One can see that even the very large calorimeter array for *IXO* yields only a relatively small FOV.

Figure 13. A solid model of the European Calorimeter Array (EURECA) focal plane. EURECA is a European-Japanese test bed for calorimeter detectors for *IXO*. The EURECA focal plane consists of a 5 x 5 TES calorimeter array and a frequency division multiplexer system. In the solid model, the detector array is in the middle and is surrounded by four filter boards for channel isolation. The four high-bandwidth SQUID output amplifiers are located in the corners (de Korte et al 2008, L. Gottardi, personal communication 2008).

Fig 1.

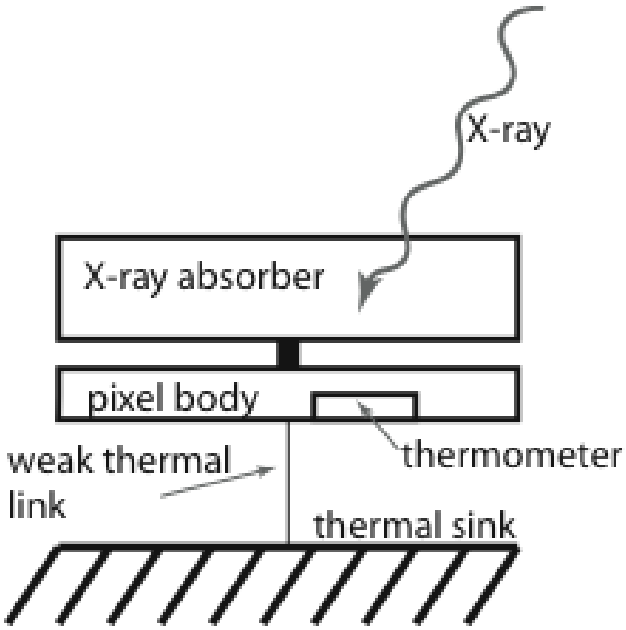
X-ray
X-ray absorber
pixel body
thermometer
weak thermal
link
thermal sink

Fig 2.

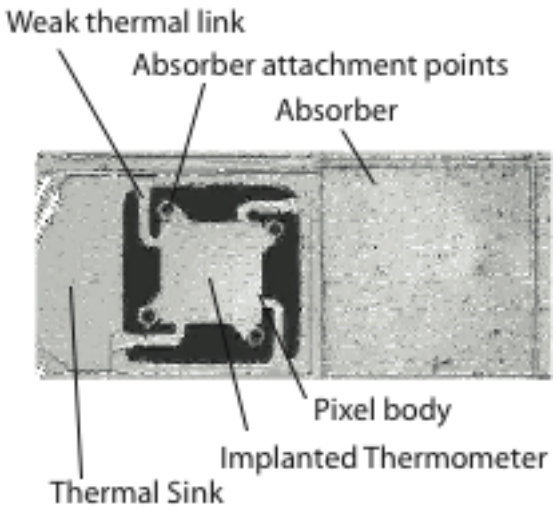
Weak thermal link
Absorber attachment points
Absorber
Pixel body
Implanted Thermometer
Thermal Sink

Fig. 3.

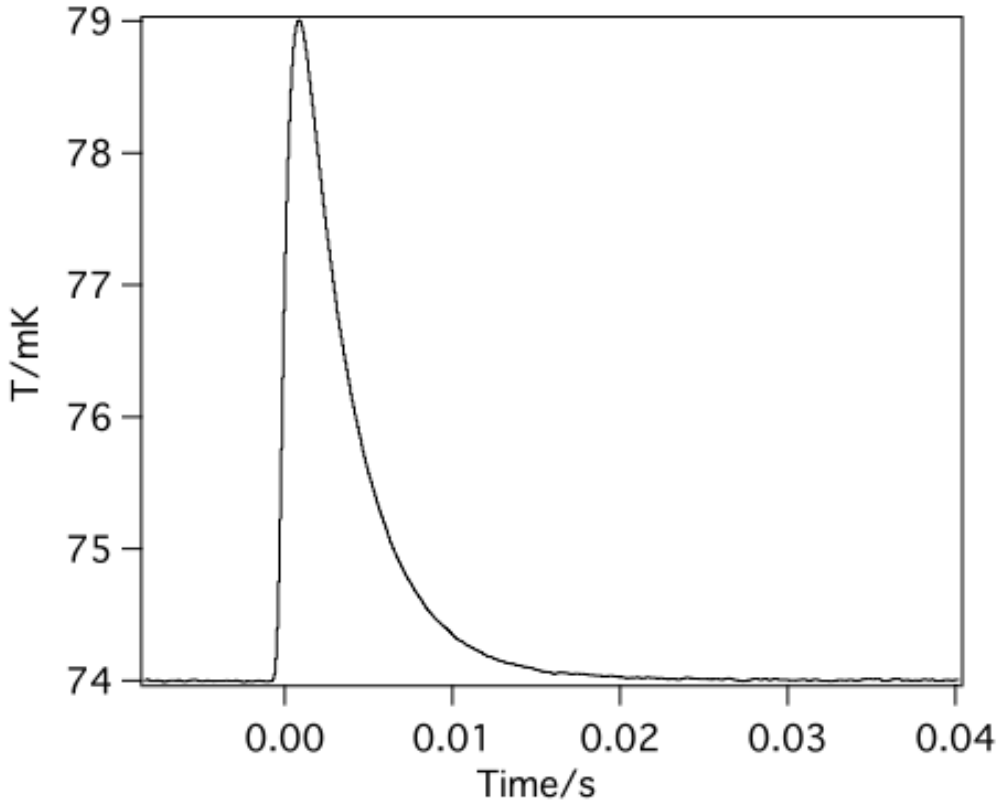

Fig. 4.

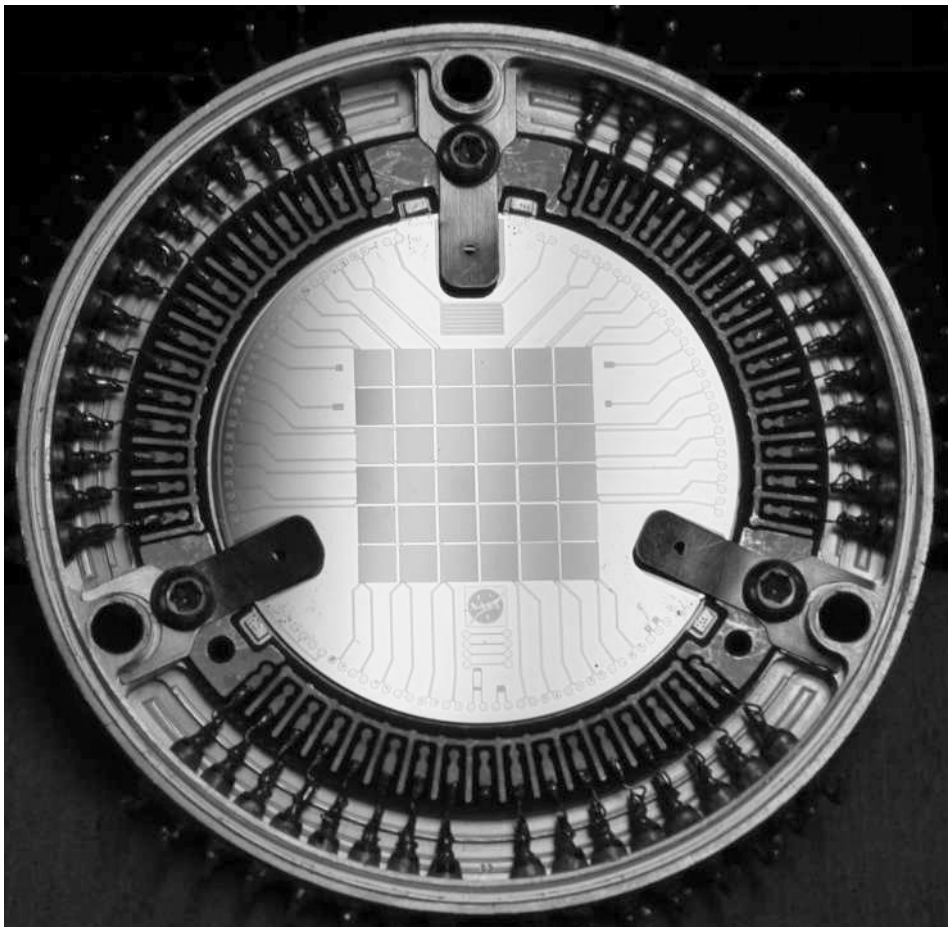

Fig 5.

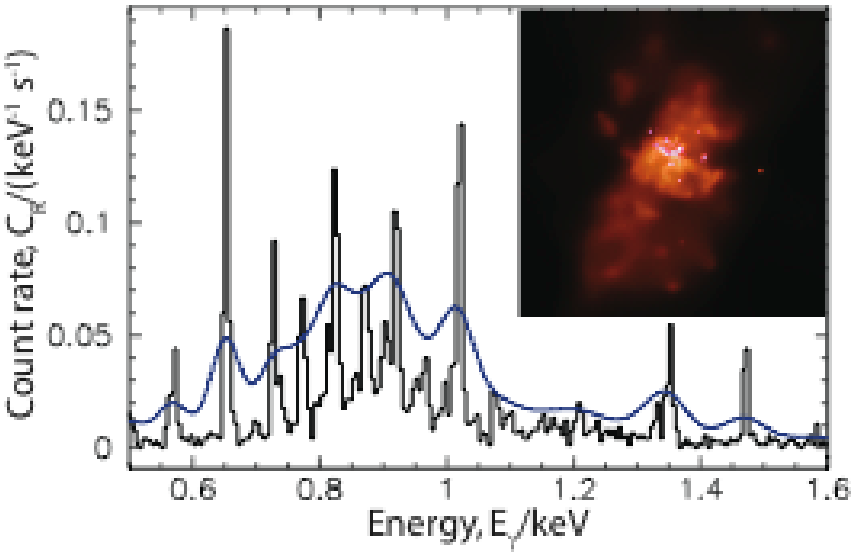
Count rate, C_E/(keV^{-1} s^{-1})
0.15
0.1
0.05
0
0.6
0.8
1
1.2
1.4
1.6
Energy, E_γ/keV

Fig. 6.

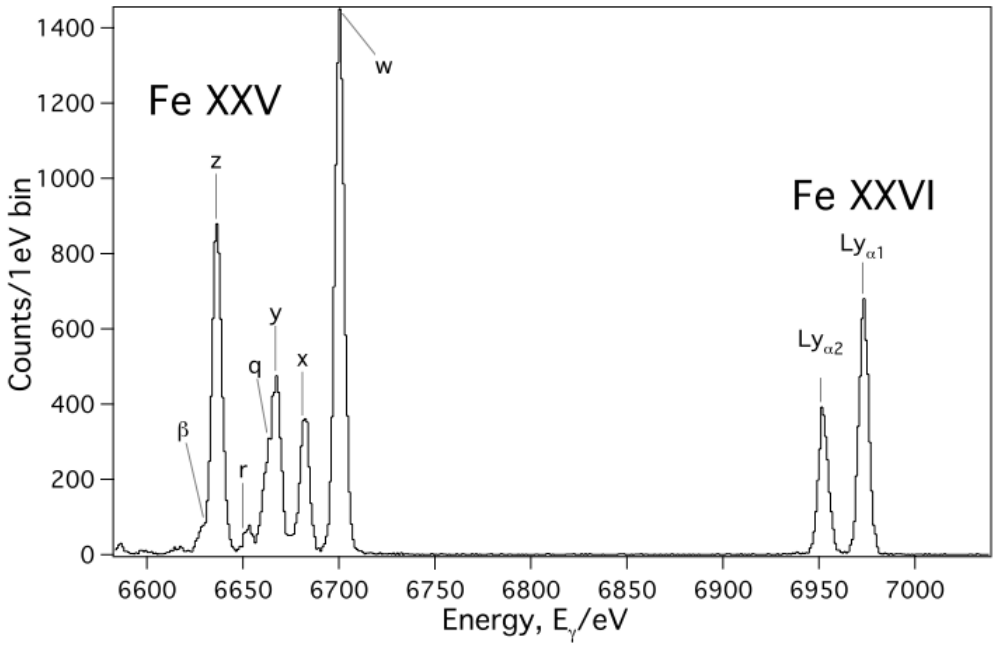
Fe XXV
Fe XXVI
w
z
y
q
x
β
r
Ly$_{\alpha1}$
Ly$_{\alpha2}$
Counts/1eV bin
Energy, E$_\gamma$/eV
0
200
400
600
800
1000
1200
1400
6600
6650
6700
6750
6800
6850
6900
6950
7000

Fig. 7.

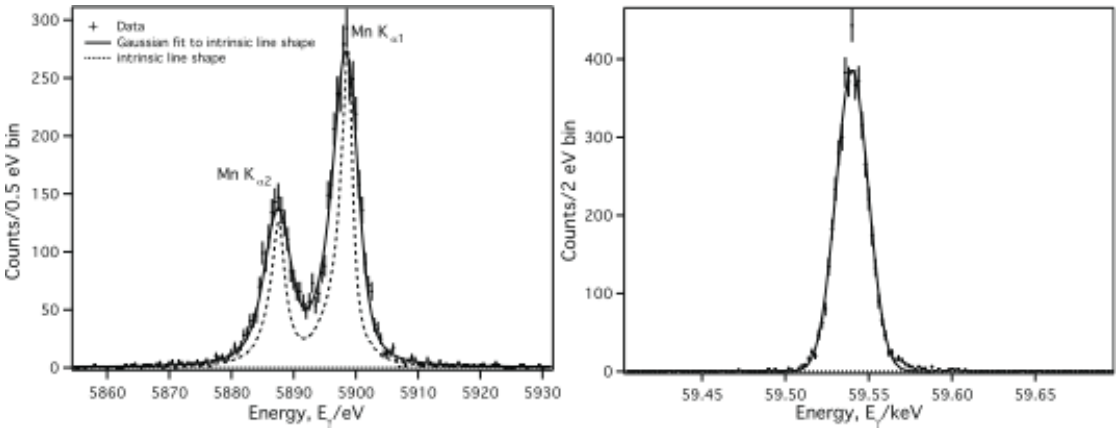
Data
Gaussian fit to intrinsic line shape
intrinsic line shape
Mn K$_{\alpha 1}$
Mn K$_{\alpha 2}$
Counts/0.5 eV bin
Energy, E$_\gamma$/eV
Counts/2 eV bin
Energy, E$_\gamma$/keV

Fig. 8.

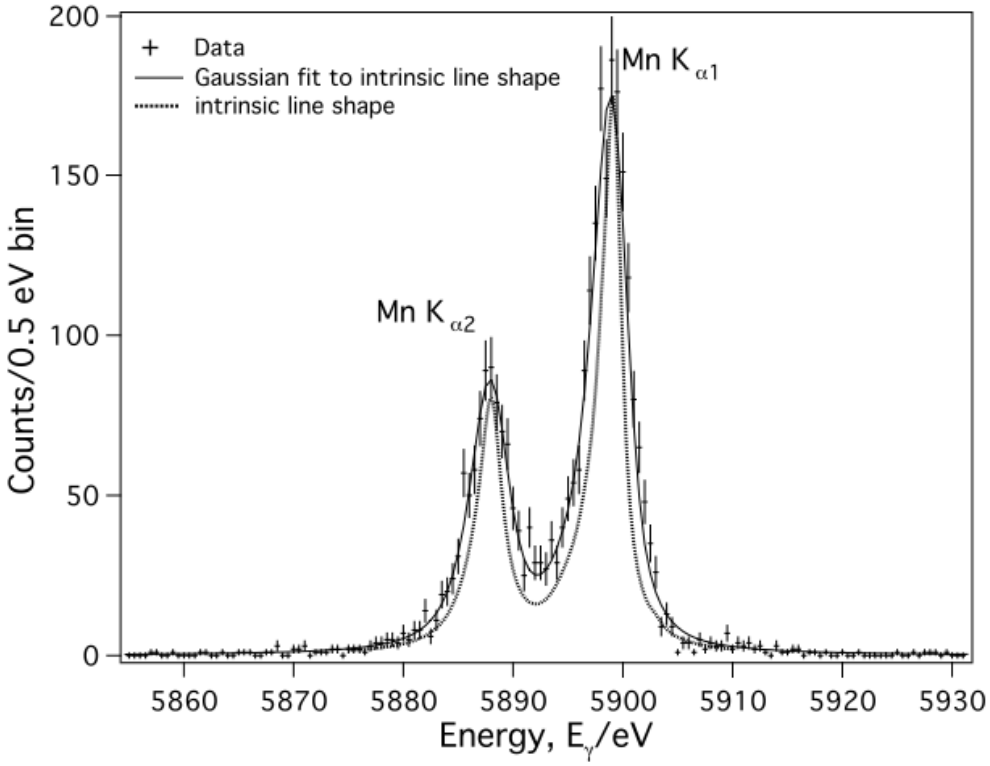
Data
Gaussian fit to intrinsic line shape
intrinsic line shape
Mn K α1
Mn K α2
Counts/0.5 eV bin
Energy, E_γ/eV
0
50
100
150
200
5860
5870
5880
5890
5900
5910
5920
5930

Fig 9.

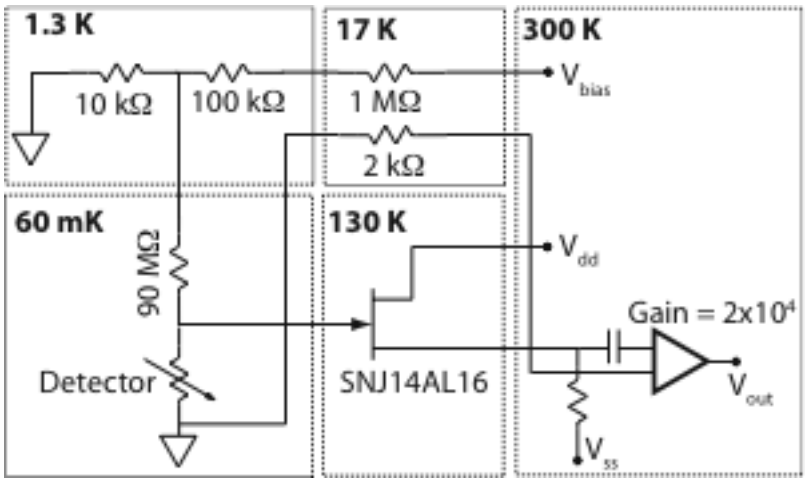
1.3 K
17 K
300 K
10 kΩ
100 kΩ
1 MΩ
2 kΩ
V bias
60 mK
130 K
90 MΩ
V dd
Gain = 2x10⁴
Detector
SNJ14AL16
V out
V ss

Fig. 10.

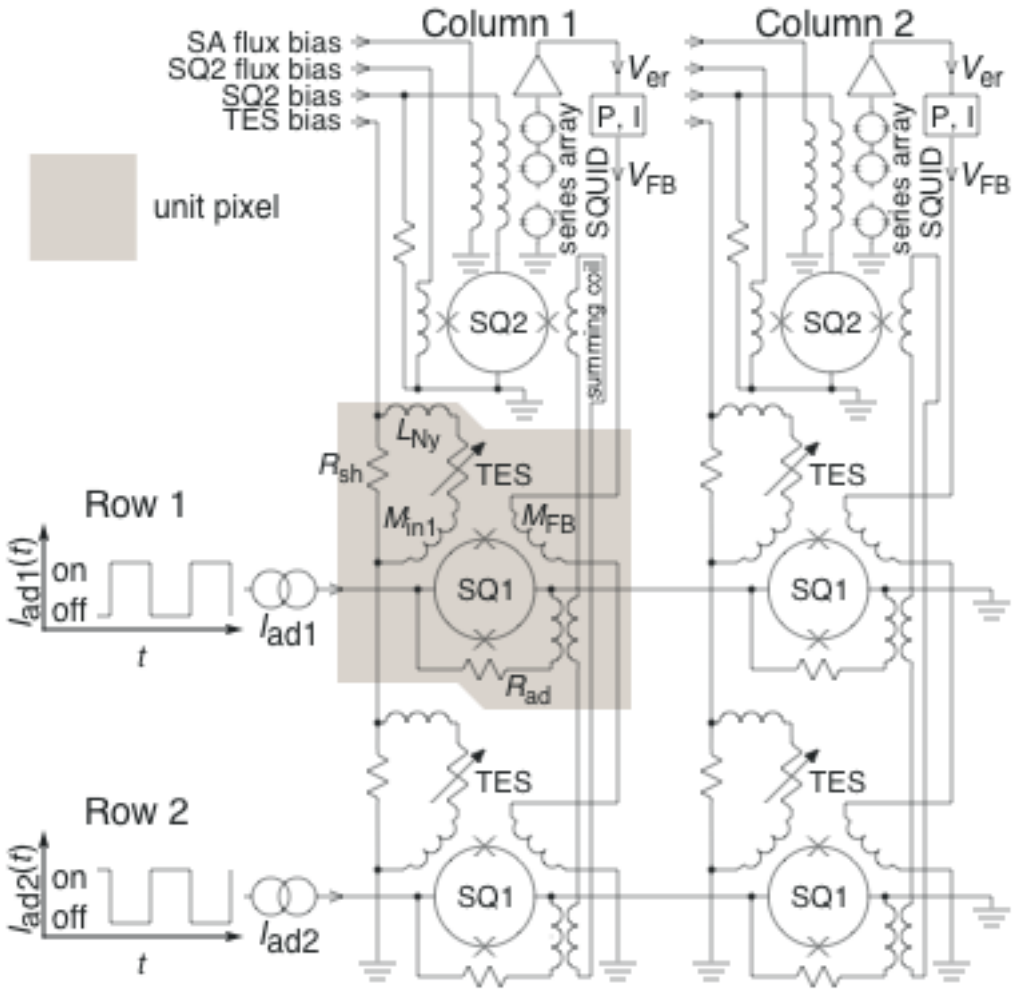
Column 1
Column 2
SA flux bias
SQ2 flux bias
SQ2 bias
TES bias
unit pixel
V_{er}
P, I
V_{FB}
series array SQUID
summing coil
SQ2
L_{Ny}
R_{sh}
TES
M_{in1}
M_{FB}
SQ1
R_{ad}
Row 1
Row 2
$I_{ad1}(t)$
$I_{ad2}(t)$
on
off
t
I_{ad1}
I_{ad2}

Fig. 11.

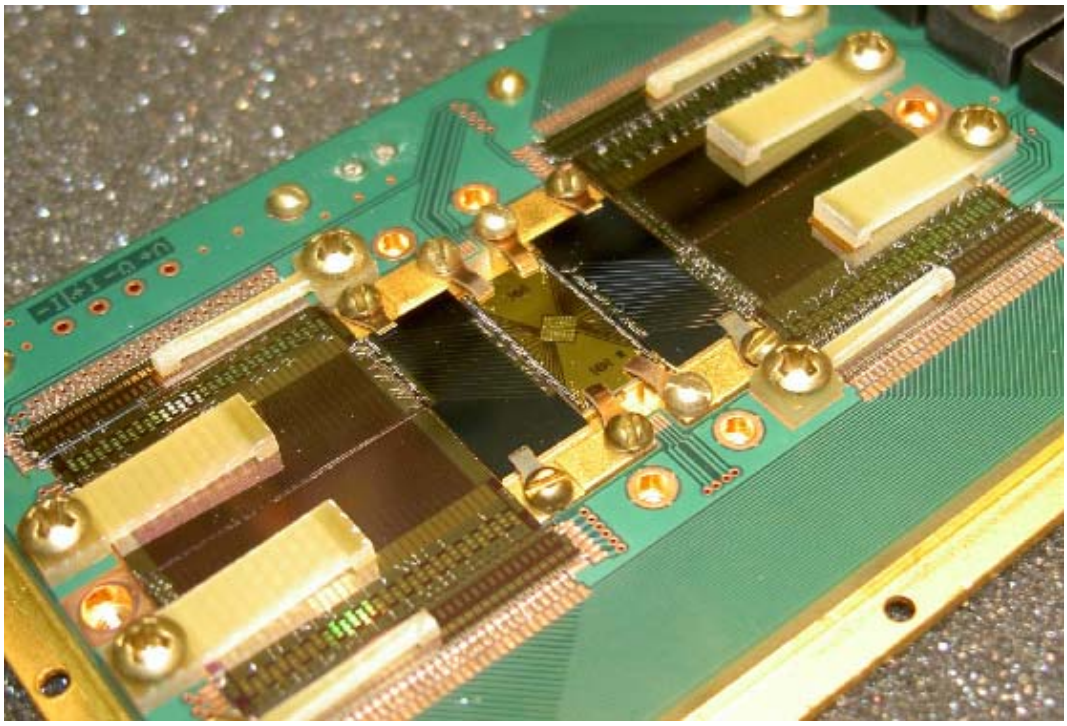

Fig. 12.

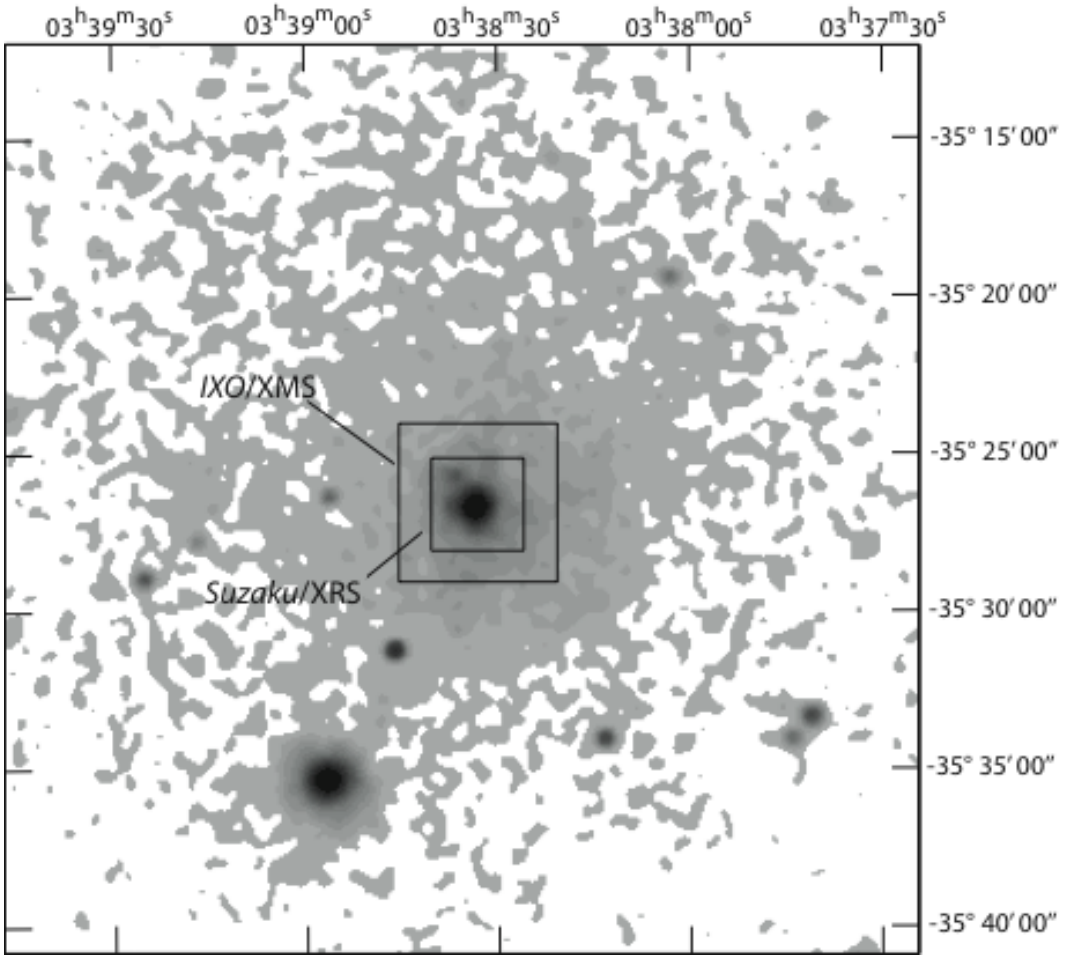
03h39m30s
03h39m00s
03h38m30s
03h38m00s
03h37m30s
-35° 15′ 00″
-35° 20′ 00″
-35° 25′ 00″
-35° 30′ 00″
-35° 35′ 00″
-35° 40′ 00″
IXO/XMS
Suzaku/XRS

Fig. 13.